

# Journal of Materials Chemistry C

Accepted Manuscript



This is an *Accepted Manuscript*, which has been through the Royal Society of Chemistry peer review process and has been accepted for publication.

*Accepted Manuscripts* are published online shortly after acceptance, before technical editing, formatting and proof reading. Using this free service, authors can make their results available to the community, in citable form, before we publish the edited article. We will replace this *Accepted Manuscript* with the edited and formatted *Advance Article* as soon as it is available.

You can find more information about *Accepted Manuscripts* in the [Information for Authors](#).

Please note that technical editing may introduce minor changes to the text and/or graphics, which may alter content. The journal's standard [Terms & Conditions](#) and the [Ethical guidelines](#) still apply. In no event shall the Royal Society of Chemistry be held responsible for any errors or omissions in this *Accepted Manuscript* or any consequences arising from the use of any information it contains.

# Regulation of Red to Near-Infrared Emission in $\text{Mn}^{2+}$ Single Doped Magnesium Zinc Phosphate Solid-Solution Phosphors by Modification of Crystal Field

Y. Y. Ma, J. Q. Hu, E. H. Song, S. Ye, Q. Y. Zhang<sup>1)</sup>

*State Key Laboratory of Luminescent Materials and Devices, and Institute of Optical Communication Materials, South China University of Technology, Guangzhou 510641, P. R. China*

## Abstract

A series of novel red to near infrared (NIR) emitting  $(\text{Mg}_{1-x}\text{Zn}_x)_{2.97}(\text{PO}_4)_2 \cdot 0.03\text{Mn}^{2+}$  ( $x = 0, 0.2, 0.4, 0.5, 0.6$  and  $0.8$ ) phosphors were prepared by a solid-state synthesis route at  $1000\text{ }^\circ\text{C}$ . The X-ray diffraction (XRD) patterns confirmed the  $(\text{Mg}_{1-x}\text{Zn}_x)_3(\text{PO}_4)_2$  solid solution phase. In addition, the characteristic photoluminescence (PL), decay times, and temperature dependent luminescence properties were investigated in detail. The different Mg/Zn ratio results in various PL intensity and spectra profile, which is related to crystal field strength and local environment of  $\text{Mn}^{2+}$  ions. The probabilities of energy transfer were discussed according to the time-resolved PL spectra. Moreover, the thermal quenching property of the samples was investigated and discussed according to the configuration coordinate diagram. The  $\text{Mn}^{2+}$  single doped phosphate  $(\text{Mg}_{1-x}\text{Zn}_x)_3(\text{PO}_4)_2$  were added to the family of phosphor applied to the light emitting diodes as well as vivo bio-imaging.

**Keywords:**  $\text{Mn}^{2+}$  ions; Near infrared; Solid solution; Photoluminescence.

---

<sup>1)</sup> Author to whom correspondence should be addressed; electronic mail: [qyzhang@scut.edu.cn](mailto:qyzhang@scut.edu.cn)

## 1. Introduction

Near infrared (NIR) emitting materials have great potential for medical diagnostics, laser system, optoelectronic device with the advantages of deep tissue penetration, high signal-to-noise ratio, maximum transparency for silicon-based optical fiber and so on.<sup>[1,2]</sup> The developing of luminescent material with strongly emission in NIR region (700-1000 nm) thus has been an attractive target. The divalent manganese ( $\text{Mn}^{2+}$ ) activated phosphors are known to be an good candidates for visible emission, which exhibit excellent optical performance.<sup>[3-8]</sup> Most recently, Song et al. demonstrate first the NIR emission in  $\text{Mn}^{2+}$ -doped fluoride perovskite originating from the super-exchange coupled  $\text{Mn}^{2+}$ - $\text{Mn}^{2+}$  pairs.<sup>[9,10]</sup> Based on the Tanabe-Sugano diagram of  $\text{Mn}^{2+}$  ion, the isolated  $\text{Mn}^{2+}$  ion can be expected to emit NIR light when the crystal field is strong enough in the case. However, the NIR emission (peaking wavelength above 700 nm), by excitation of UV/visible light, originated from the isolated  $\text{Mn}^{2+}$  has been rarely discussed before. According to the coordination chemistry and T-S diagram, it seems reasonable to speculate that the five/seven-coordinated environments for  $\text{Mn}^{2+}$  ion in favor of NIR emission generation, attributing to stronger ligand field strength (interionic distance) and weaker crystal symmetry (angular constraints) than that of four-/six-coordinated).<sup>[5-8]</sup> Therefore we start to investigate  $\text{Mn}^{2+}$  single doped compounds involving the five-coordinated for cation distributions, which may exhibit the luminescence characteristic of interest.

In order to understand the emission characteristics of  $\text{Mn}^{2+}$  in the special environments, it is desirable to study the compounds with well-defined  $\text{Mn}^{2+}$  coordination sites. In  $\gamma\text{-Mg}_3(\text{PO}_4)_2$  structure,  $\text{Mg}^{2+}$  are coordinated with five and six  $\text{O}^{2-}$  to form a distorted

polyhedron and octahedron respectively, which can afford two different crystal field for doping ions.  $\gamma$ - $\text{Mg}_3(\text{PO}_4)_2$  may offer the possible substitution positions for the  $\text{Mn}^{2+}$  ion considering the similar ionic radius between  $\text{Mg}^{2+}$  and  $\text{Mn}^{2+}$ . Accordingly,  $\gamma$ - $\text{Mg}_3(\text{PO}_4)_2$  will be a good host to be doped by  $\text{Mn}^{2+}$  ions. Moreover, the solid-solutions located between the nearly isostructural  $\gamma$ - $\text{Zn}_3(\text{PO}_4)_2$  and  $\gamma$ - $\text{Mg}_3(\text{PO}_4)_2$  yields the  $(\text{Mg}_{1-x}\text{Zn}_x)_3(\text{PO}_4)_2$  compounds. The Mg and Zn atoms are randomly distributed on the same site, and  $\text{Mn}^{2+}$  are supposed to occupy Mg and Zn sites simultaneously. Controlling the solid solubility of  $(\text{Mg}_{1-x}\text{Zn}_x)_3(\text{PO}_4)_2$  materials may be of great interest, especially when the doping cation (such as  $\text{Mn}^{2+}$ ) have luminescent properties that are sensitive to the crystal field strength and the coordination polyhedron.<sup>[11]</sup>

As a part of our research on phosphor materials, an attempt is made to synthesize a series of  $(\text{Mg}_{1-x}\text{Zn}_x)_{2.97}(\text{PO}_4)_2:0.03\text{Mn}^{2+}$  ( $x = 0, 0.2, 0.4, 0.5, 0.6$  and  $0.8$ ) solid solutions, which reveals interesting information on the  $\text{Mn}^{2+}$  emission response to varied ligand field. The different site occupation of  $\text{Mn}^{2+}$  is detailed investigated, which greatly influences the luminescent behaviors, such as emission wavelength and lifetime. In addition, the probabilities of energy transfer were discussed according to the time-resolved PL spectra. The combination of all these structural analyses and their correlation with the luminescence properties has led to an accurate understanding of the influence of thermal treatment on the cationic distribution in Mn-doped  $(\text{Mg}_{1-x}\text{Zn}_x)_3(\text{PO}_4)_2$  ( $x = 0, 0.2, 0.4, 0.5, 0.6$  and  $0.8$ ) samples.

## 2. Experimental

### 2.1. Materials and Syntheses.

The  $(\text{Mg}_{1-x}\text{Zn}_x)_{2.97}(\text{PO}_4)_2 \cdot 0.03\text{Mn}^{2+}$  ( $x = 0, 0.2, 0.4, 0.5, 0.6$  and  $0.8$ ) phosphors were synthesized by traditional high-temperature solid-state reaction. The molar concentration of  $\text{Mn}^{2+}$  ions in the solution was adjusted and fixed to be a relatively low value (1%) in this case. Stoichiometric amounts of magnesium hydroxide carbonate ( $4\text{MgCO}_3 \cdot \text{Mg}(\text{OH})_2$ , aladin, 99.99%), zinc acetate ( $\text{Zn}(\text{CH}_3\text{CO}_2)_2$ , aladin, 99.99%), ammonium phosphate basic ( $(\text{NH}_4)_2\text{HPO}_4$ , aladin, 99.99%), and manganese carbonate ( $\text{MnCO}_3$ , aladin, 99.99%) were thoroughly mixed via grinding in an agate mortar. The homogeneous mixtures of corresponding raw materials were pre-fired at  $800\text{ }^\circ\text{C}$  for 5 hours. Subsequently, the resulting powder were put into alumina crucible and sintered at  $1000\text{ }^\circ\text{C}$  for 3 hours in a horizontal tube furnace under reducing atmosphere ( $5\% \text{H}_2 + 95\% \text{N}_2$ ).

### 2.2. Characterization Method.

The structures of the final products were identified via powder XRD on a D8 Advance diffractometer with  $\text{Cu K}\alpha$  radiation ( $\lambda = 0.15406\text{ nm}$ ). The photoluminescence (PL) emission and photoluminescence excitation (PLE) spectra were measured by a steady-state fluorescence spectrometer (Edinburgh Instruments Ltd. Model FLS920) equipped with a 450-W xenon lamp as an excitation source. The emission spectrum was corrected for the spectral response of a monochromator and Hamamatsu R928P photomultiplier tube by a light diffuser. The luminescence decay curves and time-resolved photoluminescence (TRPL) spectra were measured from a spectro-fluorometer using a tunable pulse laser radiation as the

excitation. The temperature-dependent luminescence properties were measured using the same spectrophotometer which was assembled with a computer-controlled electric furnace and a self-made heating attachment.

### 3. Results and Discussions

#### 3.1. Phase analysis.

**Figure 1** displays the XRD patterns of the selected  $(\text{Mg}_{1-x}\text{Zn}_x)_{2.97}(\text{PO}_4)_2 \cdot 0.03\text{Mn}^{2+}$  ( $x = 0, 0.5$  and  $0.8$ ) solid-solution, as well as the standard pattern of  $\gamma\text{-Mg}_3(\text{PO}_4)_2$  (ICSD:31005). When  $x$  equal 0, the pure  $\gamma\text{-Mg}_3(\text{PO}_4)_2$  phase is obtained.  $\gamma\text{-Mg}_3(\text{PO}_4)_2$  crystallizes in the monoclinic space group  $P 1 21/n 1$  (No. 14), and the corresponding lattice constants of the standard pattern are as follows:  $a = 7.5957 \text{ \AA}$ ,  $b = 8.2305 \text{ \AA}$ ,  $c = 5.0775 \text{ \AA}$ ,  $\beta = 94.05^\circ$ ,  $V = 316.63 \text{ \AA}^3$ ,  $Z = 2$ . The XRD patterns recorded from the  $(\text{Mg}_{1-x}\text{Zn}_x)_{2.97}(\text{PO}_4)_2 \cdot 0.03\text{Mn}^{2+}$  ( $x = 0, 0.2, 0.4, 0.5, 0.6$  and  $0.8$ ) solid-solution series can be accordingly refined as the  $\gamma\text{-Mg}_3(\text{PO}_4)_2$  one-phase. This is conform to the previous report that the one phase nature of the compositions in the range of  $x = 0\text{-}0.8$ .<sup>[12]</sup> With the increase of  $x$ , the relative intensity of main diffracted peak of the samples continuously changed, indicating that the lattice parameter changes with the Mg/Zn ratio. **Fig. 2** plots the corresponding lattice parameters for  $a$ ,  $b$ ,  $c$  and  $V$ , which show a decrease in  $a$  and  $c$  but increase in  $b$ . Additionally, the observed anomalous variation in unit cell volume with the Mg/Zn ratio are the same as the previous paper on  $(\text{Mg,Zn})_3(\text{PO}_4)_2$  solid solutions.<sup>[13]</sup>

As shown in **Fig. 3a**, the crystal structure of  $\gamma\text{-Mg}_3(\text{PO}_4)_2$  consists of a three-dimensional framework built of distorted  $[\text{MgO}_6]$  octahedra, irregular  $[\text{MgO}_5]$

polyhedra, and nearly regular [PO<sub>4</sub>] tetrahedra that are linked together by sharing corners and edges.<sup>[14]</sup> The (Mg<sub>1-x</sub>Zn<sub>x</sub>)<sub>3</sub>(PO<sub>4</sub>)<sub>2</sub> solid-solution compounds exhibit similar crystal structures. From the consideration of the ionic charge and radius, Mn<sup>2+</sup> ( $r = 0.83 \text{ \AA}$ , CN = 6) should substitute Mg<sup>2+</sup> ions ( $r = 0.72 \text{ \AA}$ , CN = 6) or Zn<sup>2+</sup> ions ( $r = 0.74 \text{ \AA}$ , CN = 6) in (Mg<sub>1-x</sub>Zn<sub>x</sub>)<sub>3</sub>(PO<sub>4</sub>)<sub>2</sub>, because the P<sup>5+</sup> ( $r = 0.39 \text{ \AA}$ , CN = 6) are too small to accommodate the Mn<sup>2+</sup> ions.<sup>[15, 16]</sup> Furthermore, one third of the divalent cation positions in this structure type is octahedral with six-coordinated (referred as S1), while the rest are five-coordinated (referred as S2) as illustrated in **Fig. 3b** and **3c**, respectively. The S2 site preference order reported previously is identified as Zn<sup>2+</sup> >> Mg<sup>2+</sup> > Mn<sup>2+</sup>; accordingly it imply that more Mn<sup>2+</sup> ions prefer the S1 site (six-coordinated) of high zinc content sample than that of high magnesium content.<sup>[13]</sup> In addition, the average distances  $d_{S2-O}$  between S2 and O atoms in these structures ( $x = 0, 0.2, 0.4, 0.5, 0.6$  and  $0.8$ ) are calculated, which are 2.02, 2.02, 2.03, 2.04, 2.04, and 2.05 Å. Likewise,  $d_{S1-O}$  are 2.12, 2.10, 2.11, 2.14, and 2.11 Å, respectively.<sup>[13]</sup>

### 3.2. Luminescence properties of (Mg<sub>1-x</sub>Zn<sub>x</sub>)<sub>2.97</sub>(PO<sub>4</sub>)<sub>2</sub>:0.03Mn<sup>2+</sup> solid-solution

In **Fig. 4**, the PLE spectra of Mg<sub>2.97</sub>(PO<sub>4</sub>)<sub>2</sub>:0.03Mn<sup>2+</sup> exhibit several broad bands and distinct peaks within 250-600 nm, covering the NUV-Vis spectral region, which can be attributed to the transition of Mn<sup>2+</sup> ions from the <sup>6</sup>A<sub>1</sub>(<sup>6</sup>S) ground level to the <sup>4</sup>E(<sup>4</sup>D), <sup>4</sup>T<sub>2</sub>(<sup>4</sup>D), <sup>4</sup>E-<sup>4</sup>A<sub>1</sub>(<sup>4</sup>G), <sup>4</sup>T<sub>2</sub>(<sup>4</sup>G) and <sup>4</sup>T<sub>1</sub>(<sup>4</sup>G) excited levels.<sup>[17-19]</sup> When monitored at 630 and 730 nm, the normalized PLE spectra display the variant peak-position, for instance, the excitation corresponding to Mn<sup>2+</sup> <sup>6</sup>A<sub>1</sub>-<sup>4</sup>A<sub>1</sub>(<sup>4</sup>G) transition locate at 402 and 417 nm, respectively. Additionally, **Fig. 4** describes the PL spectra with different profiles for Mg<sub>2.97</sub>(PO<sub>4</sub>)<sub>2</sub>:0.03Mn<sup>2+</sup>

under 402 and 417 nm stimulation. These two asymmetric emission bands are both located at the range of 550-850 nm, which consisted of a higher- (red, peaking at 630 nm) and lower-energy (NIR, peaking at 730 nm) emission. This observation is consistent with the speculation that the  $\text{Mn}^{2+}$  ions occupy two crystallographic sites (the 5- and 6-coordination sites) in the  $(\text{Mg}_{1-x}\text{Zn}_x)_{2.97}(\text{PO}_4)_2$  host.

As expected, the two broad emission band ascribing to the spin-forbidden  ${}^4T_1({}^4G) \rightarrow {}^6A_1({}^6S)$  transition  $(\text{Mg}_{1-x}\text{Zn}_x)_{2.97}(\text{PO}_4)_2:0.03\text{Mn}^{2+}$  ( $x = 0, 0.2, 0.4, 0.5, 0.6$  and  $0.8$ ) are detected under different excitation presented in **Figs. 5a** and **5b**. When  $\lambda_{\text{ex}} = 402$  nm,  $(\text{Mg}_{1-x}\text{Zn}_x)_{2.97}(\text{PO}_4)_2:0.03\text{Mn}^{2+}$  ( $x = 0, 0.2, 0.4, 0.5, 0.6$  and  $0.8$ ) phosphors display a broad emission band peaking at about 630 nm (red, denoted as Mn(I)) and a shoulder band at about 730 nm (NIR, denoted as Mn(II)) as shown in **Fig. 5a**. To illustrate the change in the relative intensity of Mn(I) to Mn(II), the peak intensities of the Mn(I) emission band are set as the standard for each value of  $x$ . It can be seen that the emission intensity of Mn(II) reduce by increasing the composition  $x$ . In **Fig. 5b** ( $\lambda_{\text{ex}} = 417$  nm), an obvious NIR emission bands centering at 730 nm and a shoulder peak at 630 nm ( $x < 0.8$ ) can be distinguished, while the Mn(I) red emission become dominant as  $x = 0.8$ . The relative emission intensity ratio of the Mn(I) to Mn(II) increases with the increasing of the Zn content. Owing to the orientation of  $\text{Mn}^{2+}$  ions as discussed above, it can be infer that the  $\text{Mn(I)}^{2+}$  red emission originates from S1 sites (6-coordinated), meanwhile  $\text{Mn(II)}^{2+}$  NIR emission from S2 sites (5-coordinated). The position and shape of the  $\text{Mn}^{2+}$  emission bands are strongly reliant on the Mg/Zn ratio at the same excited wavelength as shown in **Fig. 5**, because the increasement (or reduction) of  $x$  value is beneficial to red (or NIR) emission.

In general, it is well known that the  $3d^5$  multiple energies of  $Mn^{2+}$  in the host lattice depends on the relevant crystal field, coordination environment, bond distances and the covalent interaction with the host lattice. According to the Tanabe-Sugano diagram used in coordination chemistry, it predicts that the energy differences between the lowest excited states  ${}^4T_1$  ( ${}^4G$ ) (and  ${}^4T_2$  ( ${}^4G$ )) and the  ${}^6A_1$  ( ${}^6S$ ) ground state of  $Mn^{2+}$  ions is extremely sensitive to the crystal-field strength  $D_q$ , and decreases with increasing of crystal field strength  $D_q$ .<sup>[20]</sup> Meanwhile, the relation between the emission energy and the mean Mg/Zn-O distance in the  $(Mg_{1-x}Zn_x)_2.97(PO_4)_2:0.03Mn^{2+}$  compounds (not making assumptions with regard to which Mg/Zn in the structure is substituted by  $Mn^{2+}$ ) is usually a function of the distance from Mg/Zn to its ligands. The  $d$ -orbital splitting of a metal center using a point charge model is given as<sup>[21,22]</sup>

$$Dq = \frac{Ze^2r^4}{6R^5} \quad (1)$$

where  $D_q$  corresponds to the energy level separation,  $Z$  is the valence of the anion ligand,  $e$  is electron charge,  $r$  is the radius of the frontier  $d$  wave-function, and  $R$  is the distance between metal center and ligand. According to the above formula,  $D_q$  is proportional to  $1/R^5$ , which imply that the bond length affect the crystal field strength significantly. With an increase in  $d_{Mg/Zn-O}$ , one may expect a decreased crystal field splitting and hence a blue shift of emission wavelength. Accordingly, the high-energy emission, as shown in **Fig. 5**, originates from the  $Mn(I)^{2+}$  ions which occupy loose crystal circumstance with larger Mg/Zn-O bond length. We thus further infer that the weak crystal field is exerted on the S1 site of six-coordinate with the longest bond length. Meanwhile, the low-energy emission originates from the  $Mn(II)^{2+}$  ions which occupy compact crystal circumstance with shorter Mg/Zn-O bond length (at S2 sites of

five-coordinate).

The luminescence decay curves of the red (Mn(I):  $\lambda_{\text{ex}} = 402$  and  $417$  nm,  $\lambda_{\text{em}} = 630$  nm) and NIR (Mn(II):  $\lambda_{\text{ex}} = 402$  and  $417$  nm,  $\lambda_{\text{em}} = 730$  nm) emissions for  $(\text{Mg}_{1-x}\text{Zn}_x)_2.97(\text{PO}_4)_2:0.03\text{Mn}^{2+}$  ( $x = 0, 0.2, 0.4, 0.5, 0.6$  and  $0.8$ ) are measured. Here, the decay curves of  $\text{Mg}_{2.97}(\text{PO}_4)_2:0.03\text{Mn}^{2+}$  and  $(\text{Mg}_{0.5}\text{Zn}_{0.5})_{2.97}(\text{PO}_4)_2:0.03\text{Mn}^{2+}$  as the examples are shown in **Fig. 6**. All the decay time of  $\text{Mn}^{2+}$  can be fitted by a second-order exponential function described as:

$$I = A_1 \exp(-t/\tau_1) + A_2 \exp(-t/\tau_2) \quad (1)$$

where  $I$  is the luminescence intensity;  $A_1$  and  $A_2$  are constants;  $t$  is the time; and  $\tau_1$  and  $\tau_2$  are the rapid and slow parts of lifetime. The average lifetime ( $\tau$ ) is presented in **Table 1**, which calculated by the following equation<sup>[23]</sup>:

$$\tau = (A_1\tau_1^2 + A_2\tau_2^2)/(A_1\tau_1 + A_2\tau_2) \quad (2)$$

The decay time of Mn(I) with red emission are measured to be 40-47 ms, while, that of Mn(II) have a shorter lifetime approximately 6-8 ms.<sup>[24]</sup> Furthermore, the results expose that the emission of Mn(I) and Mn(II) originate from different lattice sites of Mn ions, which corresponding to the inference mention above.

An overlap between the PLE spectrum of Mn(II) and the PL spectrum of Mn(I) in the range of 550-600 nm is observed, which suggest that the occurrence probability of energy transfer from Mn(I) to Mn(II). In order to obtain more information about energy transfer, the time resolved photoluminescence (TRPL) measurement are carried out. Here, we take the  $(\text{Mg}_{0.5}\text{Zn}_{0.5})_{2.97}(\text{PO}_4)_2:0.03\text{Mn}^{2+}$  as representative that the Mg/Zn ratio of which is 1:1. **Figure 7(a-g)** shows the TRPL spectra ( $\lambda_{\text{ex}} = 402$  nm,  $\lambda_{\text{em}} = 630$  nm) for

(Mg<sub>0.5</sub>Zn<sub>0.5</sub>)<sub>2.97</sub>(PO<sub>4</sub>)<sub>2</sub>:0.03Mn<sup>2+</sup> phosphors with delay time ranging from 0 to 40 ms. Each TRPL spectrum contains two distinctive Gaussian peaks, the shorter wavelength band peaking at 630 nm attributed to the 6-coordination S1 and the longer wavelength broad band at 730 nm belonged to 5-coordination S2. As shown in **Fig. 7**, the emission intensity of both two Gaussian bands continually decreases with the decay time increasing. In general, there is a process that the emission bands present firstly then reach to the maximum before the depopulation of the excited states; however, this actual procedure is not be observed in TRPL, which can be ascribed to the low-resolution of the detect instrument.<sup>[25]</sup> Here, the emission intensity of Mn<sup>2+</sup> decrease results from the depopulation are thus exhibited instead of going rise. At the primary stage ( $t = 0.4$  to  $2.5$  ms), the emission intensity ratio of Mn(I) to Mn(II) reduces with the increase of decay time. After that ( $t > 2.5$  ms), the ratio gradually increase as shown in **Fig. 7h**. As regards the downtrend of Mn(I)/Mn(II) intensity ratio, the Mn(II) emission intensity is supposed to decay faster owing to its short decay time, but the decline in the Mn(I)/Mn(II) ratio reveals the slower decay of Mn(II). For this, the specific discussion and analysis are listed in the following aspects: (i) the Mn(I) ions located at the regular site with adjacent quenching site, and susceptible to direct quenching by killer sites which are presumed to be defects or impurities in the host. This result consistent with the rapid parts of the decay lifetime as shown in **Fig. 6**. (ii) Based on the viewpoint of energy transfer, the Mn(I) (suppose to be donor) decays faster than Mn(II) (suppose to be acceptor) by the general principle.<sup>[26, 27]</sup> These facts may be considered as the evidence for the Mn(I)/Mn(II) ratio decrease. More testing and analysis (e.g. rate equation modeling) will be implemented to verify the dominant mechanism and then provide a quantitative interpretations.<sup>[28]</sup> When  $t >$

24 ms, the Mn(I) emission is dominated (see in **Fig. 7f-g**), due to the shorter lifetime of Mn(II) compared with Mn(I).

### 3.3. Thermal quenching properties of $(\text{Mg}_{0.5}\text{Zn}_{0.5})_{2.97}(\text{PO}_4)_2:0.03\text{Mn}^{2+}$

The temperature-dependent emission spectra of the  $(\text{Mg}_{0.5}\text{Zn}_{0.5})_{2.97}(\text{PO}_4)_2:0.03\text{Mn}^{2+}$  are measured to investigate the thermal quenching properties in the temperature range from 20 to 280 °C. The corresponding experimental results ( $\lambda_{\text{ex}} = 402$  and 417 nm) are shown in **Figs. 8a** and **8b**, respectively. Under 402 nm excitation, the relative intensity of Mn(I) (dominant) and Mn(II) gradually decline with increasing temperature (**Fig. 8a**). Additionally, the Mn(I) emission intensity at 150 °C reaches 94% of its initial intensity at 20 °C (seen in **Fig. 9**). In the case of  $\lambda_{\text{ex}} = 417$  nm, the peak position of the emission band for  $(\text{Mg}_{0.5}\text{Zn}_{0.5})_{2.97}(\text{PO}_4)_2:0.03\text{Mn}^{2+}$  lies at 730 nm (Mn(II)) and a peak shoulder is observed centering at 630 nm (Mn(I)) at RT as shown in **Fig 8b**. It is evident that the broad emission dramatic decrease in its intensity, while the peak shoulder intensity slightly enhance without a sharp reduction of intensity with elevation of temperature. The Mn(II) emission intensity at 150 °C only reaches its 42.6% of its initial intensity observed in **Fig 9**.

Based on the above discussion, the configuration coordinate model for the mechanism of this present case is given in **Fig. 10**. the curves AG and DG (or HK) are the ground and excited state of Mn(I) (or Mn(II)), respectively. The point F (or J) are the lowest position of excited states, and G (or K) is the crossing points of the ground and excited state of Mn(I) (or Mn(II)) ion. For Mn(I), when irradiated with the excitation light, the most of electron release the energy along the FB path to bring out the red emission. Nevertheless, since the electrons

in the intersection G position have free energy by dropping along the ground state curve rather than back to F, with the increasing temperature, a part of electron release the energy as an irradiative transition through point G. The non-radiative transition probability is strongly dependent on temperature, which may result in the decrease of emission intensity. The electrons on the excited state of  $\text{Mn}^{2+}$  get back to the ground state along the GB path have to overcome the energy barrier  $\Delta E_{FG}$  between point F and G, which determine the probability of the thermal quenching process.<sup>[29,30]</sup> Besides, after the Mn(II) absorption of excitation light, the electron jumps back along JC with NIR emission. The thermally active phonon-assisted energy transfer tunneling from the excited states of the low-energy (H) to the excited states of high-energy (D) and the intersection position K with the temperature increasing. Subsequently, the electrons on the excited state get back to ground state along path FB with red emission and the path KB without visible light following simultaneously. This may be the reason why the PL intensity of Mn(I) raise with an increase of temperature as shown in **Fig 8b**.<sup>[31]</sup> The higher  $\Delta E$ , as we known, reduces the opportunity for the electron to be lost and represents the excellent thermal quenching properties of the phosphor. According to the **Fig. 10**, the  $\Delta E_{FG} > \Delta E_{JK}$  implies that a more rapid degradation of Mn(II) emission.

#### 4. Conclusion

In summary, a series of novel red to NIR emitting  $\text{Mn}^{2+}$ -activated  $(\text{Mg}_{1-x}\text{Zn}_x)_{2.97}(\text{PO}_4)_2$  ( $x = 0, 0.2, 0.4, 0.5, 0.6$  and  $0.8$ ) solid solution are synthesized by a high-temperature solid-state reaction method. The structural features of the as-prepared samples indicate that the solubility is reached for  $0 \leq x \leq 0.8$ . The five- and six-coordinated environment for  $\text{Mn}^{2+}$

enable the generation of NIR (Mn(II): peaking at 730 nm, lower energy) and red (Mn(I): peaking at 630 nm, higher energy) emissions. It realized that the luminescence behavior of the series solid solution is mainly induced by the  $Mn^{2+}$  center positioned at different coordination states with distinct crystal field environment. The thermal quenching properties were investigated in conjunction with structural analysis. Moreover, the corresponding configuration coordinate diagram is proposed to expound this mechanism. Consequently, the solid solution technique is effective in designing appropriate phosphor that can be used in white light emitting diodes or vivo bio-imaging.

### **Acknowledgements**

This work is financially joint supported by the NSFC (Grant Nos. 51125005, and 21373259), the Fundamental Research Funds for the Central Universities (SCUT, 2015ZM034), Guangdong Natural Science Funds (2014A030306009 and 2015A030310526), and China Postdoctoral Science Foundation funded project (2014M560661).

**References**

1. A. Abdukayum, J. T. Chen, Q. Zhao and X. P. Yan, *J. Am. Chem. Soc.*, 2013, **135** (38), 14125-14133.
2. Q. H. Zhang, J. Wang, G. G. Zhang and Q. Su, *J. Mater. Chem.*, 2009, **19**, 7088-7092.
3. L. Wu, B. Wang, Y. Zhang, L. Li, H. R. Wang, H. Yi, Y. F. Kong and J. J. Xu, *Dalton Trans.*, 2014, **43**(37), 13845-13851.
4. V. B. Bhatkar, S. K. O. Omanwar and S. V. Moharil, *Physica Status Solidi a*, 2002, **191**(1), 272-276.
5. J. Yan, M. G. Brik, C. M. Liu, D. J. Hou, W. J. Zhou, B. B. Zhang, Y. Huang, Y. Tao and H. B. Liang, *Opt. Mater.*, 2015, **43**, 59-65.
6. C. J. Duan, A. C. A. Delsing, and H. T. Hintzen, *Chem. Mater.*, 2009, **21**, 1010-1016.
7. C. J. Duan, W. M. Otten, A. C. A. Delsing and H. T. Hintzen, *J. Solid State Chem.*, 2008, **181**(4), 751-757.
8. X. R. Zhong, X. P. Meng, M. Y. Li, X. Q. Wang, X. J. Wen and X. Y. Zhang, *Chem. Phys. Lett.*, 2012, **536**, 55-60.
9. E. H. Song, S. Ding, M. Wu, S. Ye, F. Xiao, S. F. Zhou and Q.Y. Zhang, *Adv. Opt. Mater.*, 2014, **2**, 670-678.
10. E. H. Song, S. Ye, T. H. Liu, P. P. Du, R. Si, X. P. Jing, S. Ding, M. Y. Peng, Q. Y. Zhang and L. Wondraczek., *Adv. Sci.*, 2015, **2**, 1500089.
11. Z. G. Xia, C. G. Ma, M. S. Molokeev, Q. L. Liu, K. Rickert, and K. R. Poepelmeier, *J. Am. Chem. Soc.*, 2015, **137**, 12494-12497.
12. J. F. Sarver, F. L. Katnack and F. A. Hummel, *J. Electrochem. Soc.*, 1959, **106**(11), 960-963.
13. A. G. Nord, *Mater. Res. Bull.*, 1980, **15**, 1183-1191.
14. A. G. Nord and P. Kierkegaard, *Acta Chem. Scandinavica*, 1968, **22**(5), 1466-1474.

15. J. Chen, Y. Liu, M. Fang and Z. Huang, *Inorg. Chem.*, 2014, **53**(21), 11396-11403.
16. S. H. Zhang, J. F. Hu, J. J. Wang and Y. Y. Li, *Mater. Lett.*, 2010, **64**(12), 1376-1378.
17. W. Lv, M. Jiao, Q. Zhao, B. Shao, W. Lu and H. You, *Inorg. Chem.*, 2014, **53**(20), 11007-11014.
18. N. Guo, H. P. You, and C. Z. Jia, R. Z. Ouyang and D. H. Wu, *Dalton Trans.*, 2014, **43**(32), 12373-12379.
19. J. Wang, S. Wang and Q. Su, *J. Mater. Chem.*, 2004, **14**(16), 2569-2574.
20. W. B. Im, N. George, J. Kurzman, S. Brinkley, A. Mikhailovsky, J. Hu, B. F. Chmelka, S. P. DenbAARS and R. Seshadri, *Adv. Mater.*, 2011, **23**(20), 2300-2305.
21. S. Shionoya and W. M. Yen. *Phosphor Handbook*, 1998, CRC Press: New York.
22. P. D. Rack and P. H. Holloway, *Mater. Sci. Eng. R.*, 1998, **21**(4), 171-219.
23. G. Blasse and B. C. Grabmaier, *Luminescent Materials*, 1994, Springer-Verlag: Berlin, New York.
24. X. Q. Xu, J. Ren, N. Huang, H. D. Zeng, G. R. Chen, D. S. Kong, C. J. Gu, C. M. Chen, Z. B. Liu, L. R. Kong and H. Z. Tao, *Opt. Mater. Exp.*, 2014, **4**(11), 2433-2440.
25. K. S. Sohn, B. H. Cho and H. D. Park, *J. Am. Ceram. Soc.*, 1999, **82**(10), 2779-2784.
26. M. Yu, J. Lin and J. Fang, *Chem. Mater.*, 2005, **17**, 1783-1791.
27. F. Liang, *Appl. Phys. A*, 2013, **115**(3), 859-865.
28. Y. W. Jung, B. H. Lee, S. P. Singh and K. S. Sohn, *Opt. Exp.*, 2010, **18**(17), 17805-17818.
29. W. Xu, G. Zhu, X. Zhou and Y. Wang, *Dalton Trans.*, 2015, **44**(19), 9241-9250.
30. L. L. Shi, H. J. Zhang, C. Y. Li and Q. Su, *RSC Adv.*, 2011, **1**(2), 298-304.
31. Z. Xia, H. Liu, X. Li and C. Liu, *Dalton Trans.*, 2013, **42**(47), 16588-16595.

**Table Caption:**

**Table 1.** Calculated decay time of each activator in the  $(\text{Mg}_{1-x}\text{Zn}_x)_{2,97}(\text{PO}_4)_2$  ( $x = 0, 0.2, 0.4, 0.5, 0.6$  and  $0.8$ ) series solid solution.

		$x = 0$	$x = 0.2$	$x = 0.4$	$x = 0.5$	$x = 0.6$	$x = 0.8$
Mn(I):	$\tau_1$ /ms	0.34	2.90	3.09	5.60	3.35	0.77
$\lambda_{\text{ex}} = 402$ nm,	$\tau_2$ /ms	48.93	46.61	43.63	49.55	50.10	48.32
$\lambda_{\text{em}} = 630$ nm	$\tau$ /ms	47.33	40.47	40.86	46.37	48.76	47.76
Mn(II)	$\tau_1$ /ms	1.15	1.14	1.01	0.12	1.33	0.32
$\lambda_{\text{ex}} = 417$ nm,	$\tau_2$ /ms	7.13	6.85	6.74	7.11	7.27	9.55
$\lambda_{\text{em}} = 730$ nm	$\tau$ /ms	6.88	6.59	6.47	6.10	6.68	8.75

**Figure Captions:**

**Figure 1.** Powder X-ray diffraction patterns for several representative  $(\text{Mg}_{1-x}\text{Zn}_x)_{2.97}(\text{PO}_4)_2:0.03\text{Mn}^{2+}$  ( $x = 0, 0.5$  and  $0.8$ ) samples and the standard pattern of  $\gamma\text{-Mg}_3(\text{PO}_4)_2$ .

**Figure 2.** Unit cell parameters of  $(\text{Mg}_{1-x}\text{Zn}_x)_{2.97}(\text{PO}_4)_2:0.03\text{Mn}^{2+}$  ( $x = 0, 0.2, 0.4, 0.5, 0.6$  and  $0.8$ ) from X-ray diffraction data show **(a)**  $a$  lattice parameter; **(b)**  $b$  lattice parameter; **(c)**  $c$  lattice parameter; and **(d)** the cell volume.

**Figure 3.** **(a)** Structure view of a unit cell of  $\gamma\text{-Mg}_3(\text{PO}_4)_2$  along  $c$ -axis, and coordination environments for Mg: **(b)** the  $[\text{MgO}_6]$  octahedron six-fold coordinated, **(c)**  $[\text{MgO}_5]$  five-fold coordinated polyhedron.

**Figure 4.** Excitation ( $\lambda_{\text{em}} = 630$  and  $730$  nm) and emission ( $\lambda_{\text{ex}} = 402$  and  $417$  nm) spectra of  $\text{Mg}_{2.97}(\text{PO}_4)_2:0.03\text{Mn}^{2+}$  phosphor.

**Figure 5.** Normalized emission spectra of  $(\text{Mg}_{1-x}\text{Zn}_x)_{2.97}(\text{PO}_4)_2:0.03\text{Mn}^{2+}$  ( $x = 0, 0.2, 0.4, 0.5, 0.6$  and  $0.8$ ) under excitation of  $402$  nm **(a)** and  $417$  nm **(b)**, respectively.

**Figure 6.** Luminescence decay curves of the Mn(I) and Mn(II) emission from the  $(\text{Mg}_{1-x}\text{Zn}_x)_{2.97}(\text{PO}_4)_2:0.03\text{Mn}^{2+}$  ( $x = 0$  and  $0.5$ ).

**Figure 7. (a-g)** Time-resolved photoluminescence spectra of  $(\text{Mg}_{0.5}\text{Zn}_{0.5})_{2.97}(\text{PO}_4)_2:0.03\text{Mn}^{2+}$  with deconvoluted Gaussian peaks at varied delay times, **(h)** the emission intensity ratio of Mn(I) to Mn(II) for  $(\text{Mg}_{0.5}\text{Zn}_{0.5})_{2.97}(\text{PO}_4)_2:0.03\text{Mn}^{2+}$  as a function of decay time.

**Figure 8.** Temperature-dependent PL spectra (**a**,  $\lambda_{\text{ex}} = 402$  nm and **b**,  $\lambda_{\text{ex}} = 417$  nm) of  $(\text{Mg}_{0.5}\text{Zn}_{0.5})_{2.97}(\text{PO}_4)_2:0.03\text{Mn}^{2+}$  phosphor under different temperatures in the range of 20-280 °C.

**Figure 9.** The emission intensity of Mn(I) ( $\lambda_{\text{ex}} = 402$  nm) and Mn(II) ( $\lambda_{\text{ex}} = 417$  nm) as a function of the temperature for  $(\text{Mg}_{0.5}\text{Zn}_{0.5})_{2.97}(\text{PO}_4)_2:0.03\text{Mn}^{2+}$ .

**Figure 10.** The configurational coordinate diagram of the ground states and the excited states of  $\text{Mn}^{2+}$  ion for  $(\text{Mg}_{0.5}\text{Zn}_{0.5})_{2.97}(\text{PO}_4)_2:0.03\text{Mn}^{2+}$ .

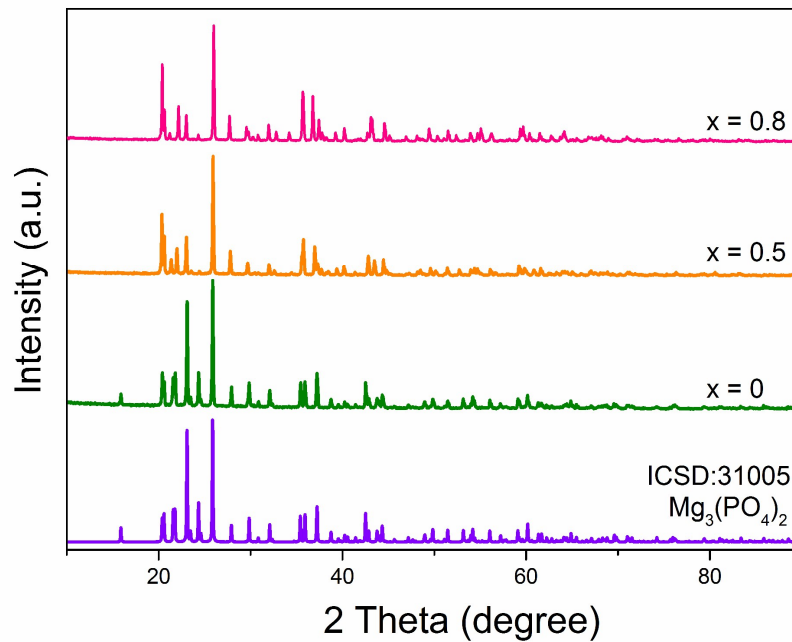


**Fig. 1.** Powder X-ray diffraction patterns for several representative  $(\text{Mg}_{1-x}\text{Zn}_x)_{2.97}(\text{PO}_4)_2:0.03\text{Mn}^{2+}$  ( $x = 0, 0.5$  and  $0.8$ ) samples and the standard pattern of  $\gamma\text{-Mg}_3(\text{PO}_4)_2$ .

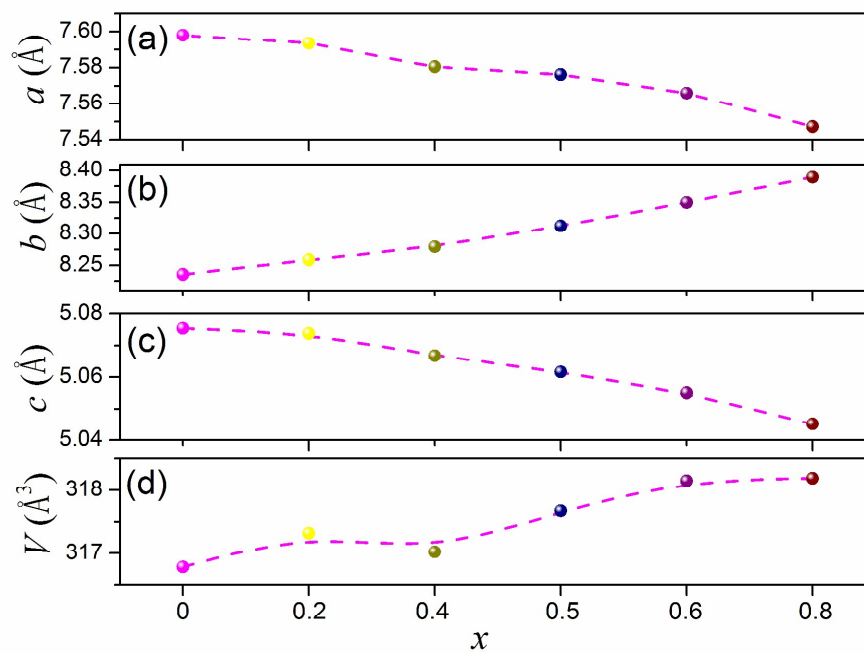


**Fig. 2.** Unit cell parameters of  $(\text{Mg}_{1-x}\text{Zn}_x)_{2.97}(\text{PO}_4)_2:0.03\text{Mn}^{2+}$  ( $x = 0, 0.2, 0.4, 0.5, 0.6$  and  $0.8$ )

from X-ray diffraction data show **(a)**  $a$  lattice parameter; **(b)**  $b$  lattice parameter; **(c)**  $c$  lattice parameter; and **(d)** the cell volume.

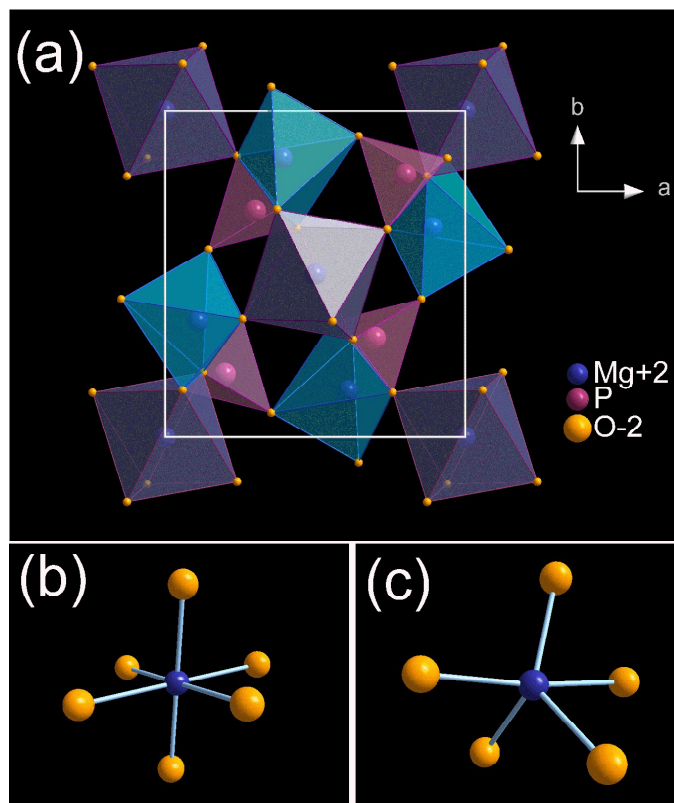


**Fig. 3.** (a) Structure view of a unit cell of  $\gamma\text{-Mg}_3(\text{PO}_4)_2$  along  $c$ -axis, and coordination environments for Mg, (b) the  $[\text{MgO}_6]$  octahedron six-fold coordinated, (c)  $[\text{MgO}_5]$  five-fold coordinated polyhedron.

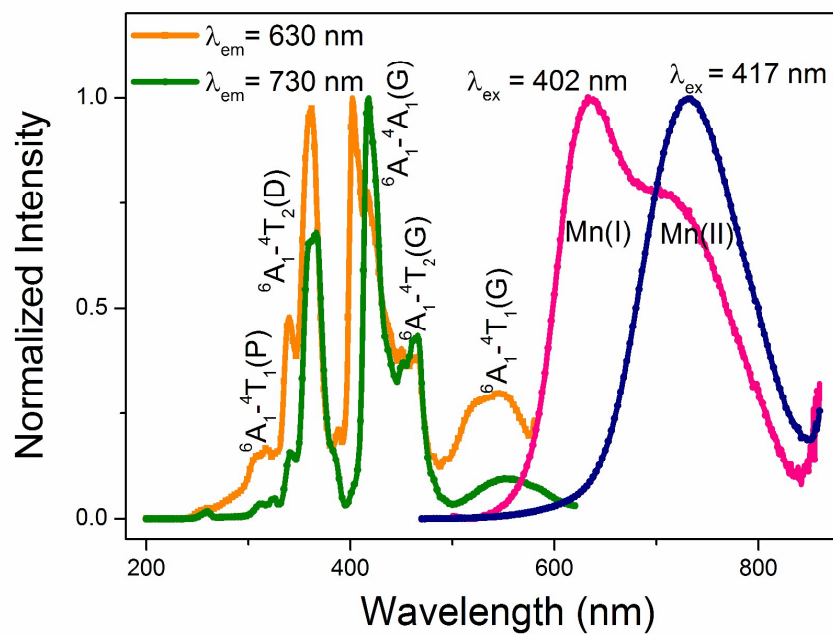


**Fig. 4.** Excitation ( $\lambda_{\text{em}} = 630$  and  $730$  nm) and emission ( $\lambda_{\text{ex}} = 402$  and  $417$  nm) spectra of

$\text{Mg}_{2.97}(\text{PO}_4)_2:0.03\text{Mn}^{2+}$  phosphor.

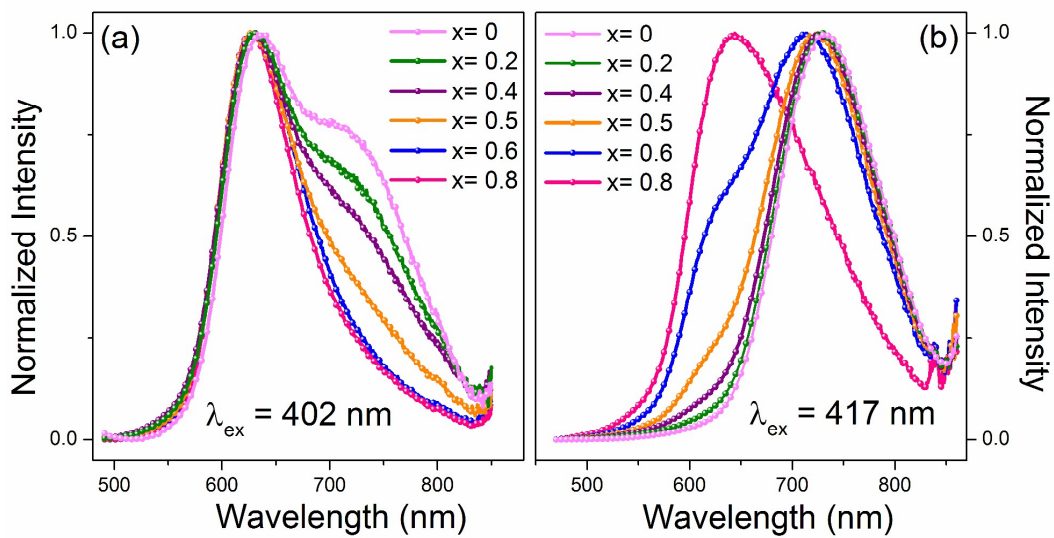


**Fig. 5.** Normalized emission spectra of  $(Mg_{1-x}Zn_x)_{2.97}(PO_4)_2 \cdot 0.03Mn^{2+}$  ( $x = 0, 0.2, 0.4, 0.5, 0.6$  and  $0.8$ ) under excitation of  $402$  nm **(a)** and  $417$  nm **(b)**, respectively.

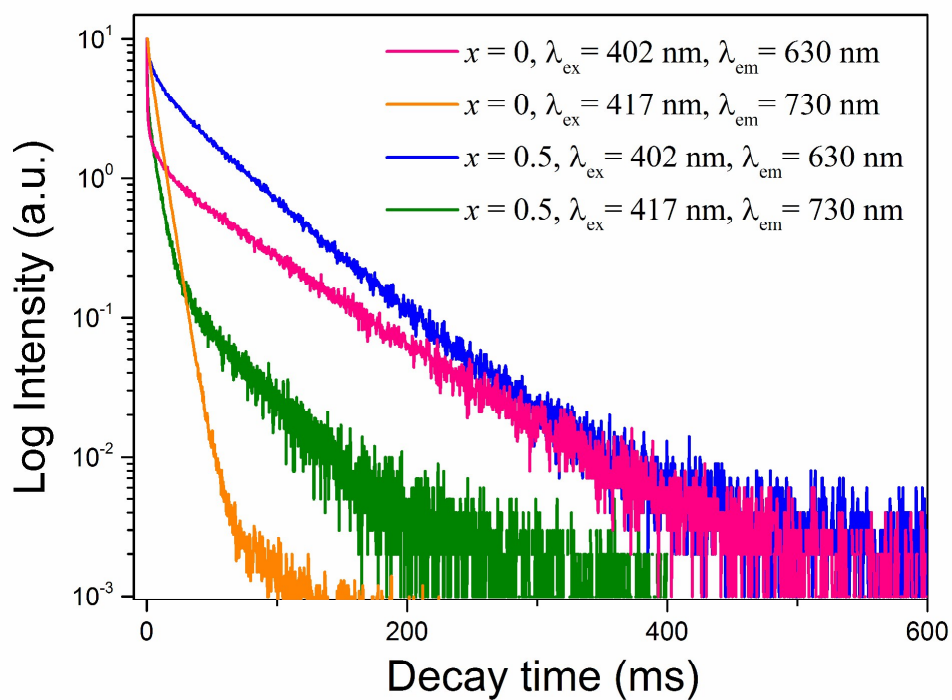
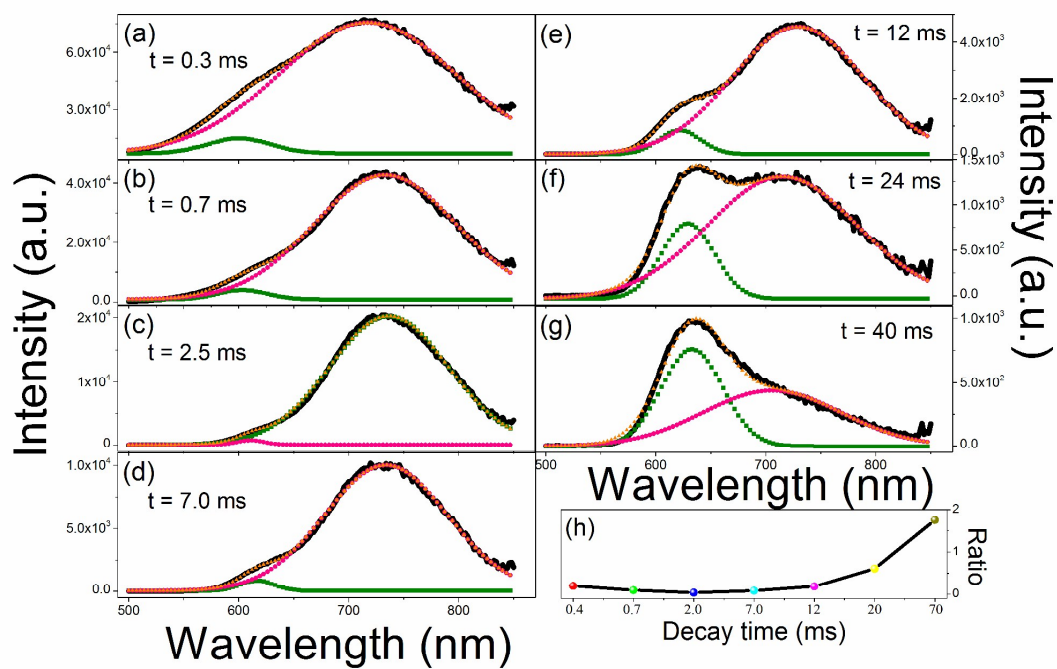
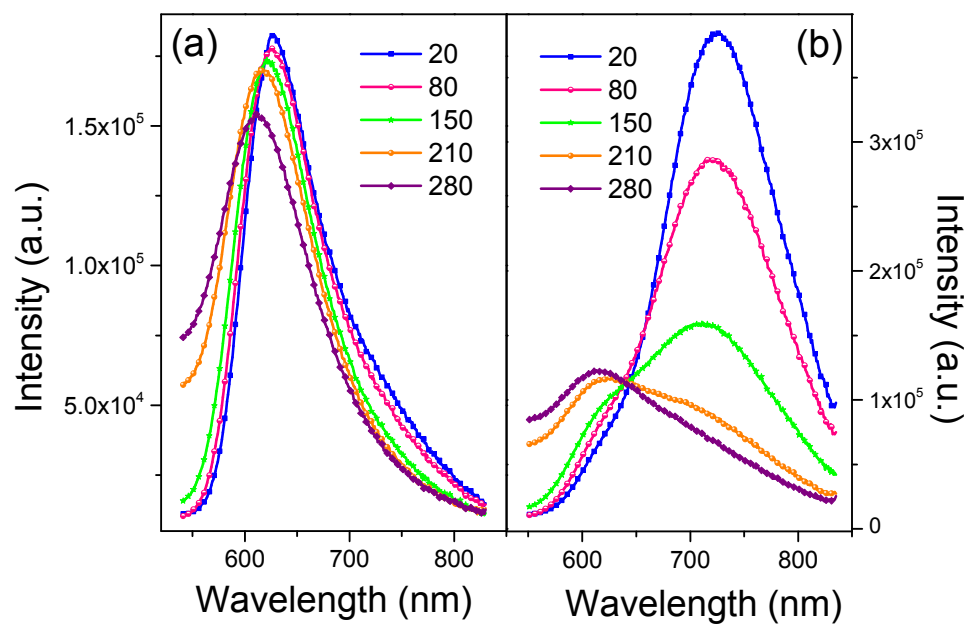


Fig. 6. Luminescence decay curves of the Mn(I) and Mn(II) emission from the





**Fig. 7.** (a-g) Time-resolved photoluminescence spectra of  $(\text{Mg}_{0.5}\text{Zn}_{0.5})_{2.97}(\text{PO}_4)_2:0.03\text{Mn}^{2+}$  with deconvoluted Gaussian peaks at varied delay times, (h) the emission intensity ratio of Mn(I) to Mn(II) for  $(\text{Mg}_{0.5}\text{Zn}_{0.5})_{2.97}(\text{PO}_4)_2:0.03\text{Mn}^{2+}$  as a function of decay time.



**Fig. 8.** Temperature-dependent PL spectra (**a**,  $\lambda_{\text{ex}} = 402$  nm and **b**,  $\lambda_{\text{ex}} = 417$  nm) of  $(\text{Mg}_{0.5}\text{Zn}_{0.5})_{2.97}(\text{PO}_4)_2:0.03\text{Mn}^{2+}$  phosphor under different temperatures in the range of 20-280 °C.

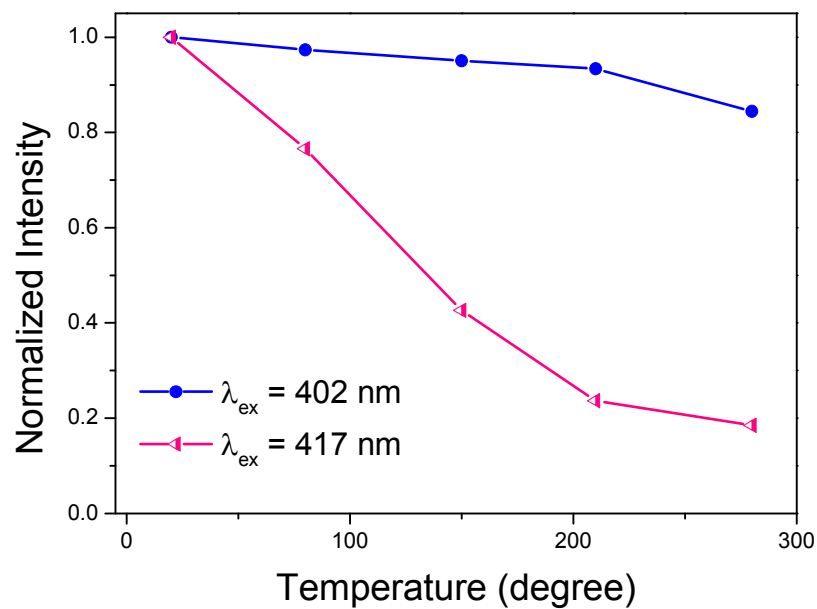


**Fig. 9.** The emission intensity of Mn(I) ( $\lambda_{\text{ex}} = 402 \text{ nm}$ ) and Mn(II) ( $\lambda_{\text{ex}} = 417 \text{ nm}$ ) as a function of the temperature for  $(\text{Mg}_{0.5}\text{Zn}_{0.5})_{2.97}(\text{PO}_4)_2 \cdot 0.03\text{Mn}^{2+}$ .

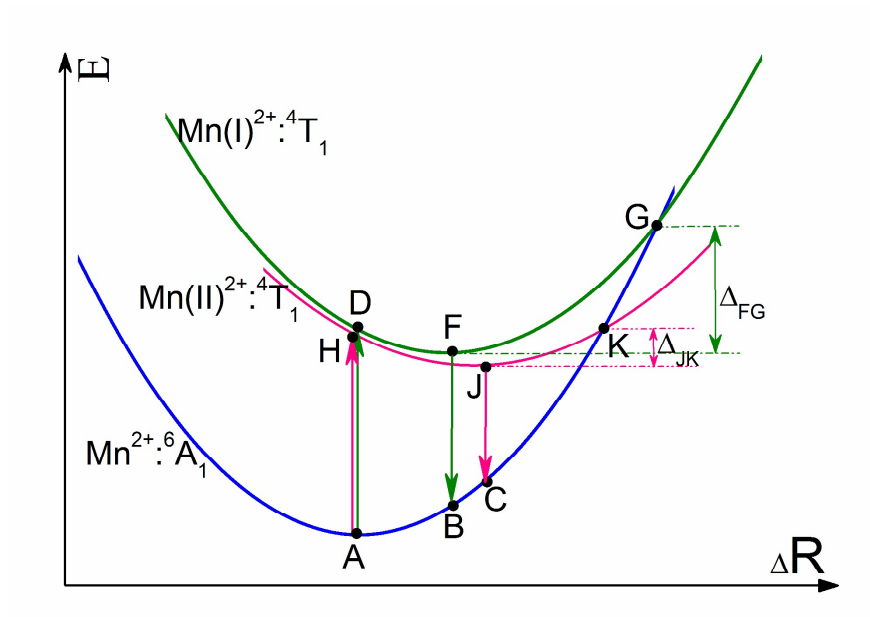
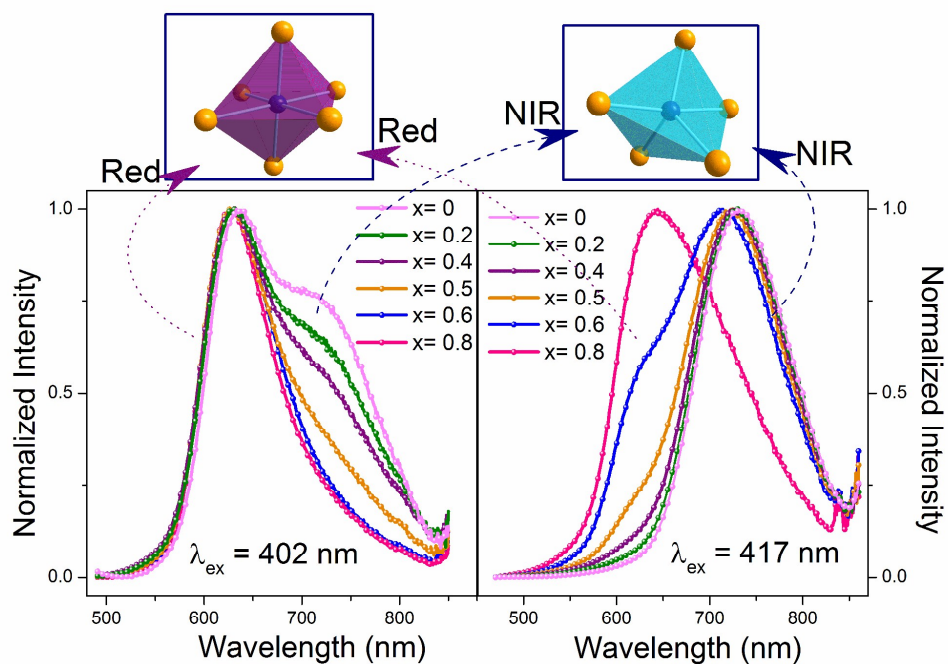


**Fig. 10.** The configurational coordinate diagram of the ground states and the excited states of

$Mn^{2+}$  ion for  $(Mg_{0.5}Zn_{0.5})_{2.97}(PO_4)_2:0.03Mn^{2+}$ .

## Graphical abstract:

TITLE: Regulation of Red-Near Infrared Luminescence in  $\text{Mn}^{2+}$  Single Doped Magnesium Zinc Phosphate Solid-Solution Phosphors by Modification of Crystal Field



A series of novel red to NIR emitting  $(\text{Mg}_{1-x}\text{Zn}_x)_{2.97}(\text{PO}_4)_2:0.03\text{Mn}^{2+}$  ( $x = 0, 0.2, 0.4, 0.5, 0.6$  and  $0.8$ ) phosphors were prepared by the solid-state synthesis route at  $1000^\circ\text{C}$ . The different Mg/Zn ratio results in various PL intensity and spectra profile, which is related to crystal field strength and local environment of  $\text{Mn}^{2+}$  ions.